Journal of The Electrochemical Society

OPEN ACCESS

Oxygen Reaction of Nonlayered Tetrahedral $KFeO_2$ Positive Electrode for Potassium-Ion Battery Using an FSA-based Ionic Liquid Electrolyte

To cite this article: Kai Jiao *et al* 2024 *J. Electrochem. Soc.* **171** 040529

Journal of The Electrochemical Society, 2024 **171** 040529

Oxygen Reaction of Nonlayered Tetrahedral $KFeO_2$ Positive Electrode for Potassium-Ion Battery Using an FSA-based Ionic Liquid Electrolyte

Kai Jiao,[1] Takayuki Yamamoto,[1,z,*] Hisao Kiuchi,[2] Haochong Zhao,[2] and Toshiyuki Nohira[1,*]

[1]*Institute of Advanced Energy, Kyoto University, Gokasho, Uji, Kyoto 611-0011, Japan*
[2]*Institute for Solid State Physics, The University of Tokyo, Kashiwa, Chiba 277-8581, Japan*

K-ion batteries (KIBs) that use ionic liquid (IL) electrolytes are promising candidates for post-Li-ion batteries because of the abundance of potassium resources and safety of ILs. We successfully synthesized stoichiometric $KFeO_2$ using a solid-state method and evaluated its charge–discharge performance as a KIB positive electrode material, with an amide-based IL electrolyte at 298 K. Transmission electron microscopy, X-ray photoelectron spectroscopy, synchrotron soft X-ray absorption spectroscopy, and energy-dispersive X-ray spectroscopy data showed that the bulk redox and surface oxidation of oxygen, rather than those of iron, contribute to the reversible and irreversible capacities, respectively. Capacity decay occurred upon repeated cycling, owing to the surface irreversible oxidation of oxygen ions to form O_2 and $K_{1-x}FeO_{2-x/2}$, which blocks the pathways of K^+ transfer to $KFeO_2$ particles. This study provides a vital platform for constructing novel KIBs and elucidates the important role of oxygen in $KFeO_2$ positive electrode.

 [DOI: 10.1149/1945-7111/ad3aab]

Manuscript submitted January 23, 2024; revised manuscript received March 15, 2024. Published April 17, 2024.

Supplementary material for this article is available online

Fossil-fuel combustion with high CO_2 production has long caused global environmental issues. Most renewable energy resources, such as wind, solar, and tidal energy resources, are intermittent, and thus, rechargeable batteries are significant energy storage media for achieving an energy sustainable society.[1] As an indispensable part of our daily lives, Li-ion batteries (LIBs) with high energy densities have been widely used in portable electronic devices over the last several decades and have emerged as prospective candidates for use in electric vehicles (EVs).[2] However, the uneven global geographical distribution of lithium and cobalt resources has resulted in price increases and further challenges to their application in large-scale energy storage systems.[3] K-ion batteries (KIBs) and Na-ion batteries (NIBs) seem to be more viable alternatives of LIBs, owing to the low standard redox potentials of sodium and potassium (Li^+/Li: −3.040 V, Na^+/Na: −2.714 V, and K^+/K: −2.936 V vs standard hydrogen electrode (SHE) in aqueous solution; $E(K^+/K) < E(Li^+/Li)$ in some non-aqueous solvents)[4,5] and abundant resources in the Earth's crust (Li: 0.0017 wt%, Na: 2.3 wt%, and K: 2.09 wt%).[6] The replacement of the Cu current collector with Al, which does not alloy with K or Na metal even at low potentials, would also reduce the cost of battery fabrication. Recent years, many efforts have been made to replace LIBs with NIBs.[7–10] However, compared to NIBs, KIBs are more attractive in terms of the availability of graphite negative electrodes.[11,12] In contrast, Na^+ ions are difficult to intercalate into graphite, limiting the application of graphite negative electrodes in NIBs.[13]

The safety issues of organic solvent electrolytes with low boiling points are also of serious concern, especially in large-scale batteries.[14] Owing to their negligible volatility and nonflammability, ionic liquids (ILs) are considered as alternatives to conventional carbonate-based electrolytes, providing an attractive and promising strategy to improve the safety of batteries.[15,16] Their outstanding physical and chemical properties for KIBs, such as wide electrochemical window and excellent thermal stability, have been widely reported.[17,18] Although it is not clear that the formation of solid electrolyte interphase (SEI) layer followed by the decomposition of electrolyte on the electrode surface is suppressed by changing organic solvent-based electrolytes to ionic liquids, our previous studies revealed that IL electrolytes conferred superior performance of various positive and negative electrodes compared with organic solvent-based electrolytes due to reductive and oxidative stability of ILs.[16,19–21] Our group developed an IL electrolyte for KIBs, namely K[FSA]–[C_3C_1pyrr][FSA] (FSA = bis(fluorosulfonyl)amide, C_3C_1pyrr = *N*-methyl-*N*-propylpyrrolidinium).[22] Further, we confirmed that when the M[FSA] molar fraction (x(M[FSA])) in M[FSA]–[C_3C_1pyrr][FSA] (M = Li, Na, K) is equal to 0.20, $E(K^+/K)$ is more negative than $E(Li^+/Li)$ and $E(Na^+/Na)$ by 0.24 and 0.35 V, respectively. These results indicate the potential of high-voltage KIBs comprising this IL electrolyte. We have also reported the high performance of negative electrode materials such as alloy-based materials[19,23] and graphite.[20,24]

The large volume change caused by K^+ insertion and extraction triggers the instability and degradation of the positive electrode during cycling. This is attributed to the relatively larger Shannon ionic radius of the K^+ ion (0.138 nm) compared to those of the Na^+ (0.102 nm) and Li^+ (0.076 nm) ions,[25] which restricts the applications of KIBs. Therefore, suitable materials are essential to improve the diffusivity of the large K^+ ions in the frame structure of positive electrode materials. To date, various positive electrode materials such as metal oxides, metal-organic frameworks, chalcogenides, organic materials, and polyanionic compounds have been reported.[26] Among them, layered transition metal oxides have attracted both scientific and practical interest because of their nontoxicity, low-cost raw materials, good structural stability, high theoretical capacity, and environmentally friendly nature. Initially, K_xMnO_2 ($0 < x < 1$) were extensively studied and showed a good electrochemical performance.[27–29] Although the practical applications of K_xMnO_2 are limited by the deficiency of K sites, a series of research on O3-, P3-, and P2-type layered transition metal oxides containing Sc, Cr, Mn, or Co were inspired by these studies.[26,30–32]

Unfortunately, there have been no reports on layered transition metal oxides with low-cost Fe. Recently, nonlayered $KFeO_2$ was fabricated and, even though it is sensitive to air (mainly moisture and

*Electrochemical Society Member.
[z]E-mail: yamamoto.takayuki.2w@kyoto-u.ac.jp

CO_2) as shown in Fig. S1, this new material is considered as a promising substitute material owing to the adoption of low-cost elements and its similar compositions to those of $LiCoO_2$.[33,34] Further, what attracts more is its stoichiometric composition, which endows $KFeO_2$ more practical value than K-deficient K_xMnO_2. In the half-cell, the capacity loss of positive electrode is compensated by the excess amount of K metal counter electrode. However, in the full cells using practical negative electrode materials such as graphite, only the K^+ ions in the positive electrode contribute to full cell capacities. The capacity loss of positive electrode directly affects the full-cell performance. In addition, unlike well-studied layered transition metal oxides with octahedral structure, nonlayered $KFeO_2$ has a three-dimensional corner-shared structure, in which Fe^{3+} coordinated by O^{2-} is located at the tetrahedral position. Such unusual structure may induce unique behaviors in the charge–discharge process. In the previous study, owing to the excellent free K^+ migration within its Fe–O skeleton, $KFeO_2$ was applied as a positive electrode material and its electrochemical performance was studied.[33] Initial charge and discharge capacities of 70 mAh g^{-1} (0.33 K^+ release) and 60 mAh g^{-1} (0.28 K^+ uptake), respectively, were obtained at 10 mA g^{-1} in the voltage range of 1.5–3.7 V of the K/$KFeO_2$ half-cell. The discharge capacity of the nonlayered $KFeO_2$ decreased to 50% of its initial capacity after 50 cycles, which was explained by the Jahn-Teller effect of Fe^{4+}. However, more sufficient evidence is needed to certify the valence of Fe change, such as X-ray photoelectron spectroscopy (XPS) or X-ray absorption spectroscopy (XAS), because it is also possible for O to play a vital role in the charge–discharge process.

Over the past several decades, transition metals have been considered to contribute to all the redox reactions of the positive electrode processes of classical layered transition metal oxides in LIBs. However, with the improvement of analysis method and equipment, recent studies have questioned this simple hypothesis and found that oxygen also exhibits strong electrochemical activity that allows it to participate in Li^+ insertion and extraction reactions in the positive electrode, thereby contributing to notable increases in the capacity.[35–39] Several mechanisms such as the reversible lattice oxygen redox reaction,[40,41] O_2 gas evolution,[42] and associated surface reactions[43] have been reported, of which the contributions of reversible O redox and irreversible O oxidation have been distinguished.[44] Similarly, in the cases of O3-type layered $NaFeO_2$ positive electrode in Na-ion batteries (NIBs)[45] and layered $K_{0.4}Mn_{0.5}Fe_{0.5}O_2$ positive electrode in K-ion batteries (KIBs),[46] the oxygen redox reaction, instead of the redox reaction of Fe^{3+}/Fe^{4+}, was found to compensate the charge balance for reversible charge–-discharge reactions. In addition, $K_{0.4}Mn_{0.5}Fe_{0.5}O_2$ shows moderate cycling stability,[46] whereas $KFeO_2$ shows rapid capacity decay.[33] As mentioned above, the formation of Fe^{4+} in $KFeO_2$ positive electrode, which was suggested in the previous study,[33] needs to be more clarified experimentally. If O contributes the reversible capacity instead of the formation of Fe^{4+}, some other interesting reactions should be responsible for the capacity decay of $KFeO_2$.

Above all, the development of cost-effective positive electrode materials with safe and superior potassium storage performance is an ongoing research pursuit. In this study, nonlayered tetrahedral $KFeO_2$ was synthesized using the solid-state method and its charge–discharge behavior as a positive electrode material for KIBs in K[FSA]–[C_3C_1pyrr][FSA] IL electrolyte was investigated. Further, more detailed mechanism of K^+ insertion and desertion into $KFeO_2$ and capacity decay were discussed.

Experimental

Synthesis of $KFeO_2$.—All materials and reagents were of analytical grade and were used as received without further purification. Fe_2O_3 (FUJIFILM Wako Pure Chemical Corp., 99.9% purity) and 20 mol% excess K_2CO_3 (Sigma-Aldrich, 99.0% purity) were mixed in an agate mortar. The mixture was then calcined in a tubular furnace at 1173 K for 12 h under argon gas to obtain the $KFeO_2$ samples. Owing to the sensitivity and instability of $KFeO_2$ to moisture (Fig. S1), the as-synthesized $KFeO_2$ was naturally cooled in argon gas flow and ground for 20 min in an open dry chamber to avoid the contact with moisture after calcination. Finally, the ground powder was transferred to an Ar-filled glovebox (H_2O, $O_2 < 0.5$ ppm) for storage until further use.

Material characterization.—The elemental compositions of the $KFeO_2$ powder were determined using inductively coupled plasma atomic emission spectrometry (ICP-AES; Spectroblue, Hitachi). The optical morphologies of $KFeO_2$ powder unexposed and exposed in air for 4 h were observed by microscope (VHX 7100, Keyence). The morphologies and elemental mapping images were obtained using scanning electron microscopy (SEM; Phenom Pro Generation 5, Thermo Fisher Scientific) coupled with energy-dispersive X-ray spectroscopy (EDS, SE1200–8001, Thermo Fisher Scientific,). For as-synthesized $KFeO_2$ powder, SEM analysis was performed after coating the surface of the as-synthesized $KFeO_2$ with Au to improve its conductivity. Prior to SEM analysis, the $KFeO_2$ powder and electrode were inevitably exposed to air for several seconds. The powder X-ray diffraction (XRD) patterns of the $KFeO_2$ powder and electrodes at different charge–discharge states were obtained using an X-ray diffractometer (Ultima IV, Rigaku, Cu-$K\alpha$ radiation $\lambda = 1.5418$ Å) over the 2θ range of 10°–80° with a scan speed of 2° min^{-1}. Rietveld refinement was performed using RIETAN-FP software.[47] The crystal structures were drawn by using VESTA system.[48] X-ray photoelectron spectroscopy (XPS) was employed to detect the valance states of Fe and O with K^+ insertion and extraction after mild argon-ion etching $KFeO_2$ electrodes to remove surface impurities, using a spectrometer with Mg-$K\alpha$ radiation (JPS-9010, JEOL). The electronic structure evolution of $KFeO_2$ was characterized by ex situ synchrotron-based soft X-ray absorption spectroscopy (sXAS) at the Fe L-edge and O K-edge at BL-11 of the SR center (Ritsumeikan University, Japan). In addition, focused ion beam scanning electron microscopy (FIB-SEM; SMF2000, Hitachi) and transmission electron microscopy (TEM; JEM-ARM200F, JEOL) were employed to characterize the crystal structure of pristine $KFeO_2$, its crystal structure changes, and the elemental distributions of the different charge–discharge states. To completely avoid exposure of the $KFeO_2$ powder and electrodes to air and moisture during XRD, FIB-SEM, and TEM analyses, the samples were treated in an argon-filled glovebox and transferred to the corresponding instruments in airtight vessels. The electron diffraction indexes were determined by using CrysTBox software.[49]

Electrochemical measurements.—The working electrode was prepared by pressing a mixture of active material (85 wt%), acetylene black (10 wt%), and poly(tetrafluoroethylene) (5 wt%) onto an Al mesh in an Ar-filled glove box. The amount of active material loaded in each electrode was approximately 8.5 mg cm^{-2}. The materials were evaluated as positive electrodes in CR2032-type coin cells with potassium metal (Sigma-Aldrich, 98% purity) as the counter electrode. The electrolyte was prepared by dissolving K[FSA] (Nippon Shokubai Co., Ltd., purity ⩾99%) salt into [C_3C_1pyrr][FSA] (Kanto Chemicals Co., Ltd.) ionic liquid to be a molar composition of x(K[FSA]) = 0.20 (x: molar fraction). A two-ply glass fiber filter (Whatman, GF/A, thickness: 260 μm) was used as the separator. The cell assembly was performed in a glovebox filled with dry and deoxygenated argon. The galvanostatic charge–discharge tests were carried out using a potentiostat (580-type battery cycler, Scribner Associations, Inc.) at voltage ranges of 2.5–3.7 V and 2.5–3.6 V at 298 K. The cyclic voltammetry (CV), galvanostatic intermittent titration technique (GITT), and electrochemical impedance spectroscopy (EIS) were applied by using a potentiostat (VSP, Biologic Co.). CV curves were recorded at a scan rate of 0.1 mV s^{-1} in the voltage range of 2.5–3.7 V. GITT measurements were performed by applying a constant current rate of 10 mA g^{-1} for 30 min, followed by 2 h rest period (open circuit). For EIS measurement, in order to remove the large resistance of K metal, coin cells were fabricated with two $KFeO_2$ electrodes, which were prepared by cycling for 1 or 10 cycles at 10 mA g^{-1} using K/$KFeO_2$

half-cells in advance. Then, after $KFeO_2$/$KFeO_2$ symmetric coin cells were kept at 0 V for 10 min, EIS measurement was performed with an amplitude of 20 mV in the frequency range of 200 kHz to 100 mHz. For ex situ XRD, XPS, sXAS and TEM experiments, the cells were disassembled in the glovebox after charging and discharging to certain voltages.

Results and Discussion

The elemental compositions of the as-synthesized $KFeO_2$ were characterized as K/Fe = 0.88, 0.94, and 1.01 for 5%, 10%, and 20% excess K_2CO_3, respectively, as determined by inductively coupled plasma atomic emission spectrometry (ICP-AES) (Table S1). Notably, an unknown peak appears at ~45° (Fig. S2) when less than 5% excess K_2CO_3 was used for calcination. Stoichiometric $KFeO_2$ was successfully synthesized by adding 20% excess K_2CO_3 to the raw material. As shown in Fig. 1a, XRD measurement coupled with Rietveld refinement determines that $KFeO_2$ has a crystal structure with the space group *Pbca* in an orthorhombic unit cell. The $KFeO_2$ crystal lattice is formed by three-dimensional corner-sharing FeO_4 tetrahedra (inset of Fig. 1a) and its lattice constants are refined as $a = 5.6076(7)$ Å, $b = 11.252(2)$ Å, $c = 15.940(2)$ Å, and $R_{wp} = 2.23\%$. The refined parameters are provided in table S2. The crystal structure of $KFeO_2$ was elucidated using transmission electron microscopy (TEM), as shown in Fig. 1b, wherein the selected-area electron diffraction (SAED) pattern corresponds to a single crystal of $KFeO_2$ that is well assigned to the diffraction indices of 124 and 164. In addition, the surface morphology and elemental distributions of $KFeO_2$ were characterized by scanning electron microscope (SEM) and energy-dispersive X-ray spectroscopy (EDS), as shown in Figs. 1c–1f. SEM analysis revealed that $KFeO_2$ is composed of agglomerated particles in the size range of 1–2 μm, whereas EDS mapping revealed that K, Fe, and O are uniformly distributed over the $KFeO_2$ particles. The relative atomic percentages of K and Fe in the EDS spectra (Fig. S3) are consistent with the ICP-AES results.

The electrochemical performance of the as-synthesized $KFeO_2$ was evaluated using coin cells with K metal as the counter electrode.

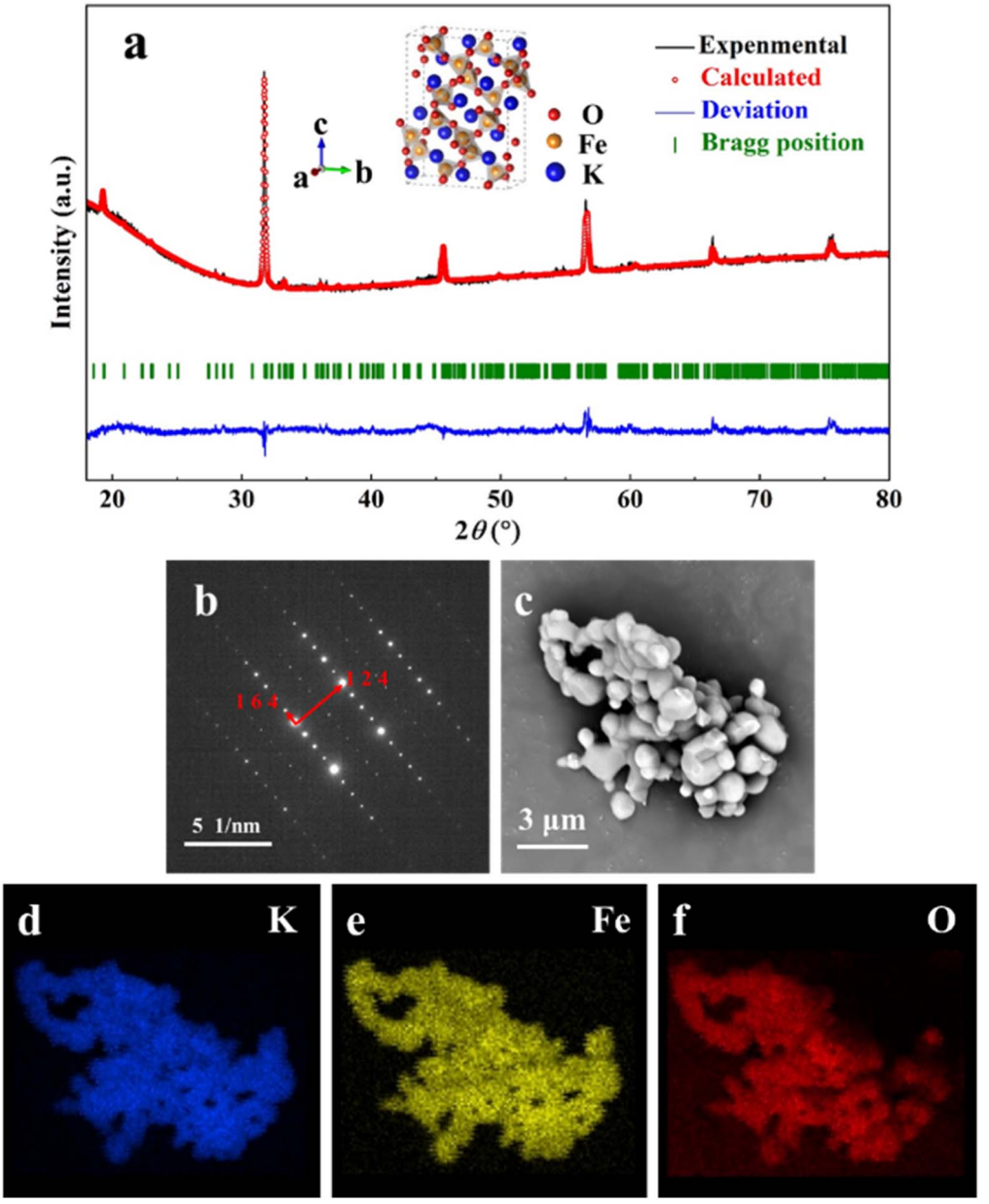

Figure 1. (a) XRD pattern and schematic illustration of as-synthesized $KFeO_2$ powder. (b) TEM image and the corresponding selected-area electron diffraction (SAED) patterns. (c) SEM images and (d)–(f) elemental mapping of the individual elements.

Figs. 2a and 2b show the charge–discharge curves and cycling performance of a $KFeO_2$ electrode at 10 mA g^{-1} in the voltage range of 2.5–3.7 V at 298 K. $KFeO_2$ delivers initial charge and discharge capacities of 47.3 mAh g^{-1} (0.22 K^+ insertion) and 44.3 mAh g^{-1} (0.21 K^+ extraction), respectively, with a coulombic efficiency of 93.7%. In the first two cycles, $KFeO_2$ exhibits good cycle stability with slight discharge capacity decay. However, the $KFeO_2$ electrode displays a decreasing discharge capacity from the fifth cycle and the average coulombic efficiency of the $KFeO_2$ electrode is kept around 95%. Consequently, a discharge capacity of only 19.7 mAh g^{-1}, commensurate with 44.5% of the value observed in the first cycle, is maintained after 30 cycles, which corresponds to an average capacity decay of 1.9% per cycle. When the voltage range is set at 2.5–3.6 V, the $KFeO_2$ electrode exhibits more stable charge and discharge curves, although its reversible capacity becomes lower (Fig. S4). Under this condition, the initial charge and discharge capacities of $KFeO_2$ are 38.9 and 35.9 mAh g^{-1}, respectively, with a capacity retention of 63.5% after 30 cycles.

To determine the reasons for the observed capacity decay, the structural evolution of $KFeO_2$ was studied using ex situ XRD analysis, at various charge and discharge states during the first cycle. As shown in Figs. 2c and 2d, no impurity peaks appear during the charge and discharge processes of the first cycle. Similar results are observed at the second cycle (2.5–3.7 V) and even after charging to 4 V (Fig. S5). Although $KFeO_2$ maintains almost the same diffraction pattern throughout the cycling experiment, the intensity of the main $KFeO_2$ peak at ~31.9° continues to decrease, and a prominent shoulder peak remains during discharging. The main peak intensity of $KFeO_2$ in the fully discharged state is lower than that of the pristine sample, thereby indicating a slight irreversible decrease in the crystallinity of $KFeO_2$. Thus, we speculate that this incomplete reversible structural evolution may be the cause of the gradual capacity decay during cycling (Fig. 2a). In contrast, for the voltage range of 2.5–3.6 V (Fig. S4), no prominent shoulder peak is observed after discharging to 15 mAh g^{-1}, leading to more stable performance and higher capacity retentions. Surface SEM observation was employed to characterize the microstructure change of $KFeO_2$ positive electrode after 10 cycles in the voltage range of 2.5–3.7 V and 2.5–3.6 V, as shown in Fig. S6. Although the pristine electrode looks denser compared to the cycled electrodes, no clear difference was observed in the two $KFeO_2$ electrodes after cycling at different cut-off voltages. In addition, ex situ XPS was employed to determine the charge compositions of $KFeO_2$ at different charge–discharge states after etching to remove surface impurities (see Fig. S7). In the Fe $2p_{3/2}$ region, the $KFeO_2$ electrodes in the pristine and all charge–discharge states present a prominent peak at a binding energy of ~710 eV, corresponding to the presence of trivalent iron. This negligible shift in the binding energy indicates that almost no redox reaction occurs with the iron atom in the voltage range of 2.5–3.7 V. Conversely, a slight shift in the binding energy is observed in the O 1s region. During charging and discharging, the O 1s peak is negatively shifted by approximately 1 eV. Although the origin of this behavior is not clear at this moment, it might be contributed by the formation of different oxygen bond of iron oxide-based compounds with K^+ insertion and extraction, and/or by the formation of a cathode electrolyte interphase (CEI) on the electrode surface. To further understand the kinetic mechanism of $KFeO_2$ during charge–discharge process, CV, GITT and EIS tests were performed as shown in Figs. S8, S9 and S10. Fig. S8 indicates the reversible redox behavior with almost overlapped CV curves in the initial 3 cycles, which is consistent with the charge–discharge curves (See Fig. 2a). Also, GITT test was adopted

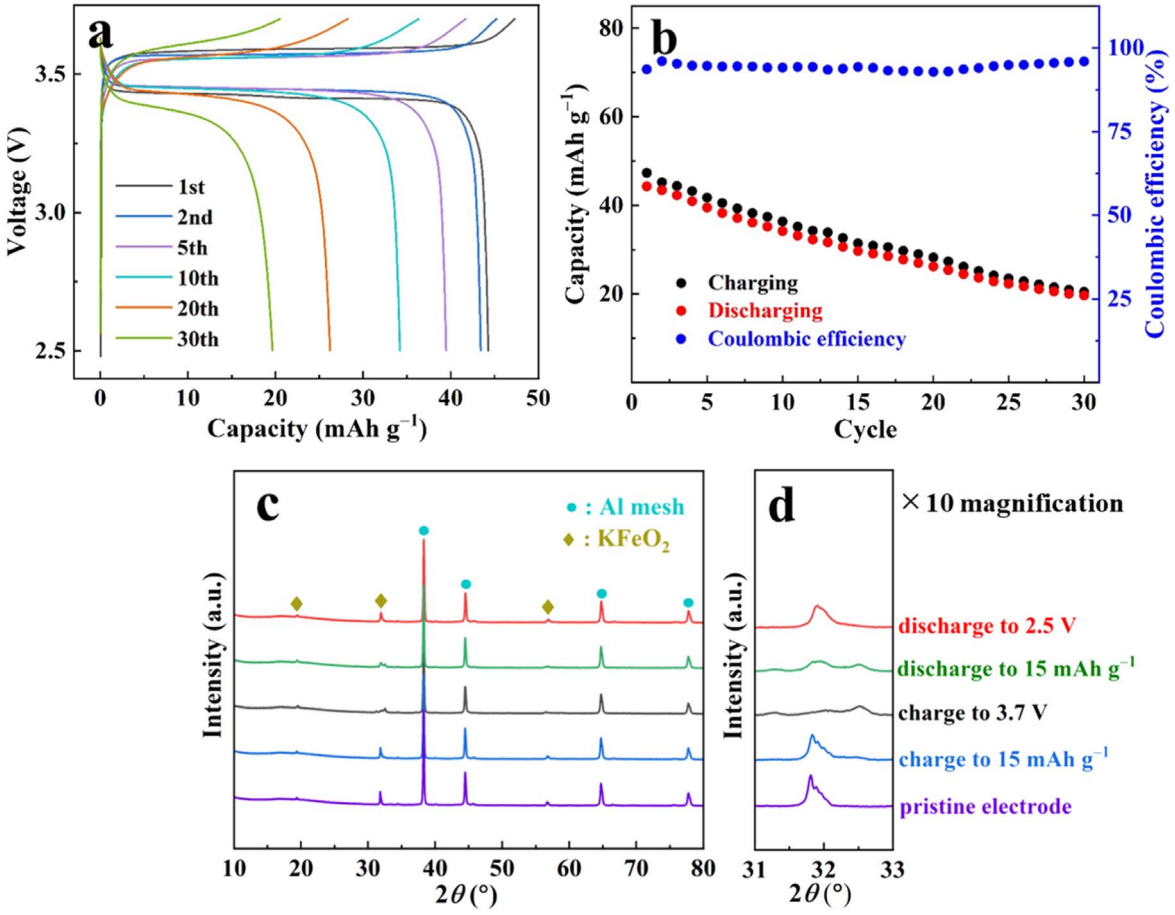

Figure 2. (a) Galvanostatic charge–discharge curves and (b) cycling performance of a $KFeO_2$ electrode across 30 cycles at 10 mA g^{-1} in the voltage range of 2.5–3.7 V at 298 K. (c), (d) XRD patterns of the different stages in the first cycle of the galvanostatic charge–discharge profiles.

to estimate the chemical diffusion coefficient of K^+ ions (D_{GITT}), as shown in Fig. S9. If the transport of K^+ ion obeys Fick's second law, D_{GITT} was calculated according to the equation as follows:[50,51]

$$D_{GITT} = \frac{4}{\pi\tau}\left(\frac{m_B V_m}{M_B S}\right)^2\left(\frac{\Delta E_s}{\Delta E_t}\right)^2 (\tau \ll L^2/D_{GITT}) \quad [1]$$

where τ is the duration of the current pulse (30 min), V_m and M_B are its molar volume and molecular weight, m_B is the mass of the active material, S is the geometric surface area (0.15 cm^2), ΔE_s is the difference in the open circuit voltage measured after a current pulse for two successive steps, ΔE_t is the voltage change during the single titration current pulse, and L is the thickness of electrode. This equation can be applied when there is a linear correlation between E and $t^{1/2}$. The D_{GITT} values of most titration steps are calculated to be in the range of 10^{-10} to 10^{-12} cm^2 s^{-1}, which is in good agreement with the common D_{GITT} values of positive electrode materials for KIBs.[52,53] Finally, EIS analysis was adopted to make a comparison for the electrodes after 1 and 10 cycle charge–discharge, as shown in Fig. S10. Each EIS spectrum shows a semicircle region, which typically corresponds to the surface resistance including the charge-transfer resistance and the surface film (CEI). The EIS spectrum shows that the surface resistance of $KFeO_2$ electrode after 10 cycles is slightly larger than that of electrode after 1 cycle, which may lead to the capacity degradation within 10 cycles.

Soft X-ray absorption spectroscopy (XAS) is a widely used method for probing the different oxidation states of the transition metal (Fe, Mn, etc.) L-edge and the chemical bond information of the low atomic number element (O, etc.) K-edge during the charging and discharging processes.[54] Particle depth information—outermost surface (3 nm), surface (10 nm), and bulk (100 nm)—on the electronic structures of the transition metal element Fe and light element O reactions can be effectively obtained with different detection modes of soft XAS, including the partial electron yield (PEY), total electron yield (TEY), and partial fluorescence yield (PFY) modes.[55] Figures 3a and 3b show the bulk information of the Fe L-edge and O K-edge of $KFeO_2$ in different charge and discharge states, respectively. There are almost no energy shifts in the Fe L-edge peaks with the insertion and extraction of K^+ into $KFeO_2$ according to the soft XAS measurements in the PFY mode. Owing to the effect of the cubic crystal field, the five Fe 3d orbitals of the tetrahedrally coordinated $KFeO_2$ lose their degeneracy and split into three t_{2g} and two e_g orbitals. The splitting energy of tetrahedral $KFeO_2$ (Δ_{tet}) is lower than that of the octahedron (Fig. 3c),[56] and thus, only one undivided pre-edge peak is observed in the energy range of 704–710 eV (Fig. 3a). For O (Fig. 3b), the pre-edge peak in the energy range of 527–530 eV is assigned to a hybridization of the Fe 3d–O 2p sub-bands, whereas the higher energy range of 532–540 eV is ascribed to a hybridization of the Fe 4sp–O 2p sub-bands.[45] Owing to the low splitting energy of the tetrahedral coordination, the O K-edge also shows an undivided pre-edge peak in the energy range of 527–530 eV. Fig. 3d shows the schematic crystal structure and electronic configurations of the Fe^{3+} and Fe^{4+} ions with high-spin state in the Fe 3d–O 2p orbitals of $K_{1-x}FeO_2$. Here, the hybridization of the Fe 3d–O 2p sub-bands results in ligand field splitting and mixing of the O 2p orbitals into the Fe 3d sites, which is named as highly covalent.[57] Purple O can be a substitute active electron donor by sharing a ligand hole with Fe to form green Fe^{4+} (Fe 3d5L^{4+}, where L is the ligand hole shared by O), as confirmed in previous studies.[45,58] A peak reversibly appears at approximately 526 eV at the full charged state of 3.7 V. This is assigned to the formation of the unstable O^{n-} species by providing a ligand hole to Fe^{3+} and substituting it to lose electrons. Hence, we believe that O, rather than Fe, contributes to the redox reaction and reversible capacity during cycling.

Figures 3e and 3g show that compared to those of the pristine $KFeO_2$ electrode, there are almost no higher energy shifts of the Fe L-edge peaks with the insertion and extraction of K^+ into $KFeO_2$ in all TEY and PEY modes, which indicates no redox reaction with Fe. With a corner-shared tetrahedral structure, the $KFeO_2$ electrodes at all charging and discharging states afford different Fe L-edge XAS spectra from those of α-Fe_2O_3,[59–61] γ-Fe_2O_3,[45] and Fe_3O_4,[60,61] all of which belong to the octahedral structure. The shoulder peak of the pristine electrode at ~705 eV, which is similar to that of tetrahedral $FePO_4$,[62] is assigned to the tetrahedral structure of Fe^{3+}. This shoulder peak shows an irreversible small increase in relative intensity to the main peak at ~706.8 eV. Besides, another shoulder peak appears at around 707.5 eV during charging and discharging. The above results suggest the irreversible transformation to octahedral Fe^{3+} and the increase in splitting energy of t_{2g} and e_g orbitals.[57,63]

Conversely, Figs. 3f and 3h show different spectral shapes around the O K-edge for the pristine, charged, and discharged states. A prominent peak (peak B) irreversibly appears at ~534 eV at the charged and discharge states. Similar peaks at around 535 eV have been observed for both tetrahedral and octahedral Fe^{3+} compounds;[64,65] however, considering the changes confirmed in Fe L-edge spectra on the surface region (Figs. 3e and 3g), it is likely to correspond to the irreversible structural transformation from tetrahedral to octahedron-containing compounds. Similar to bulk process, O^{n-} species also form on the particle surface. Then, in contrast to the bulk particle, the as-formed O^{n-} species decompose to form O^{2-} and O_2 or CO_2 (formed by the reaction with the electrolyte). For example, in the $NaFeO_2$ system used as a positive electrode for sodium-ion batteries, CO_2 release (indicates O_2 evolution from the octahedral $NaFeO_2$ lattice) and octahedral Fe_3O_4 formation have been reported after charging to 4.5 V.[45] However, there is no evidence to certify the formation of Fe^{2+} in this study. Thus, it is likely that a part of the tetrahedral $KFeO_2$ is transformed to an octahedron-containing Fe^{3+} compound, $K_{1-x}FeO_{2-x/2}$, after charging to 3.7 V. The irreversible structural transformation of $KFeO_2$ from a corner-shared FeO_4 tetrahedron to an FeO_6 octahedron possibly blocks the pathways of K^+ diffusion into $KFeO_2$ from the electrolyte and further results in capacity decay with cycling.

To further investigate this mechanism, TEM, SEM, and EDS analyses were performed to examine the variation in the structural characteristics and elemental distributions of the bulk and surface $KFeO_2$ electrodes when charged to 3.7 V (Figs. 4a and 4b), 4.5 V (Figs. 4c and 4d), and discharged to 2.5 V after charging to 3.7 V (Figs. 4e and 4f). Figure S11 shows the low magnification TEM images of a single-particle $KFeO_2$ in the corresponding charge–-discharge states. In contrast to Figs. 4a, 4c, and 4e, intragranular cracks can be observed in all three states, which appear with charging to 3.7 and 4.5 V and clearly decrease after discharging to 2.5 V, owing to the extraction and insertion of K^+ into the $KFeO_2$ particles. According to the surface SEM images (Figs. 4b, 4d, and 4f), the charged and discharged $KFeO_2$ particles exhibit multilayer structures. The EDS analysis reveals the elemental distributions from the surface to the bulk of the $KFeO_2$ particles. We assume that Fe is an unlikely component of the CEI formed by the decomposition of the electrolyte. According to the elemental distribution of Fe from surface to bulk (EDS curve slopes of the Fe intensity), the surface is composed of CEI- and $K_{1-x}FeO_{2-x/2}$-dominant layers, respectively. For the discharged sample (Fig. 4f), the Fe concentration reaches a maximum in the surface layer, which most likely indicates pure $K_{1-x}FeO_{2-x/2}$. Assuming the reversible formation of $KFeO_2$ at the discharged state in the bulk (K:Fe:O = 1:1:2), the composition of $K_{1-x}FeO_{2-x/2}$ is calculated to be $K_{0.52}FeO_{1.72}$ from the EDS curves (Figs. 4g and S12). Evidently, K^+ is further extracted from the $KFeO_2$ structure, and the O_2 evolution reaction is also promoted at high voltages (charging to 4.5 V), which causes more distinct microstructural evolution of $KFeO_2$. The thicknesses of the CEI-dominant layer at the outermost surface and inner $K_{1-x}FeO_{2-x/2}$ layer are approximately 8 and 14 nm, respectively, when the sample was charged to 3.7 V. These thicknesses increase up to 15 and 36 nm, respectively, with further charging to 4.5 V (Fig. 4d), and pure CEI is observed because of no Fe signal of EDS curve in the most surface layer. For the sample discharged to 2.5 V

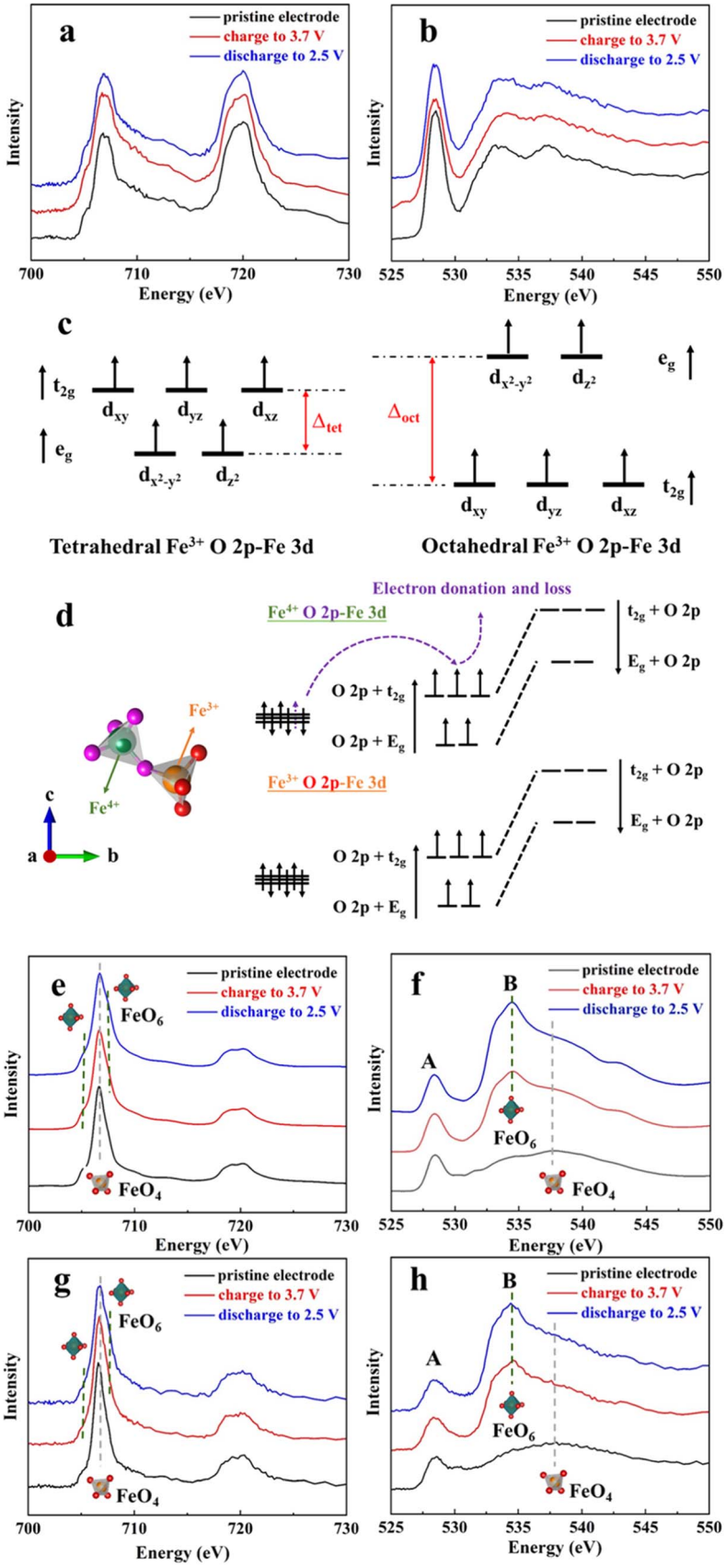

Figure 3. Ex situ soft XAS spectra at the (a) Fe L-edge and (b) O K-edge of the $KFeO_2$ electrodes at the different states in the first cycle of the galvanostatic charge–discharge profiles under partial fluorescence yield mode (PFY), which affords the bulk information of the samples. (c) Schematic of O 2p and Fe 3d orbital splitting in Fe^{3+} tetrahedral and octahedral structures. (d) Schematic crystal structure and electronic configurations of high-spin state Fe^{3+} and Fe^{4+} in $K_{1-x}FeO_2$. Ex situ soft XAS spectra at the (e), (g) Fe L-edge and (f), (h) O K-edge of the different stages in the first cycle of the galvanostatic charge–-discharge profiles under total electron yield (TEY, e and f) mode and partial electron yield (PEY, g and h), which provide the surface information and outermost surface of the samples, respectively.

(2.5–3.7 V operation, Fig. 4f), the thicknesses of the CEI- and $K_{1-x}FeO_{2-x/2}$-dominant layers (5 and 16 nm) are almost maintained. These results indicate the irreversible formation of $K_{1-x}FeO_{2-x/2}$, leading to capacity decay with cycling. Figure S13 describes the EDS mapping results of a $KFeO_2$ particle at different charge–-discharge states, which indicates the uniform elemental distributions of K, Fe, and O. In addition, Fig. S14 shows that all bulk SAED patterns at the different charge and discharge states correspond to a

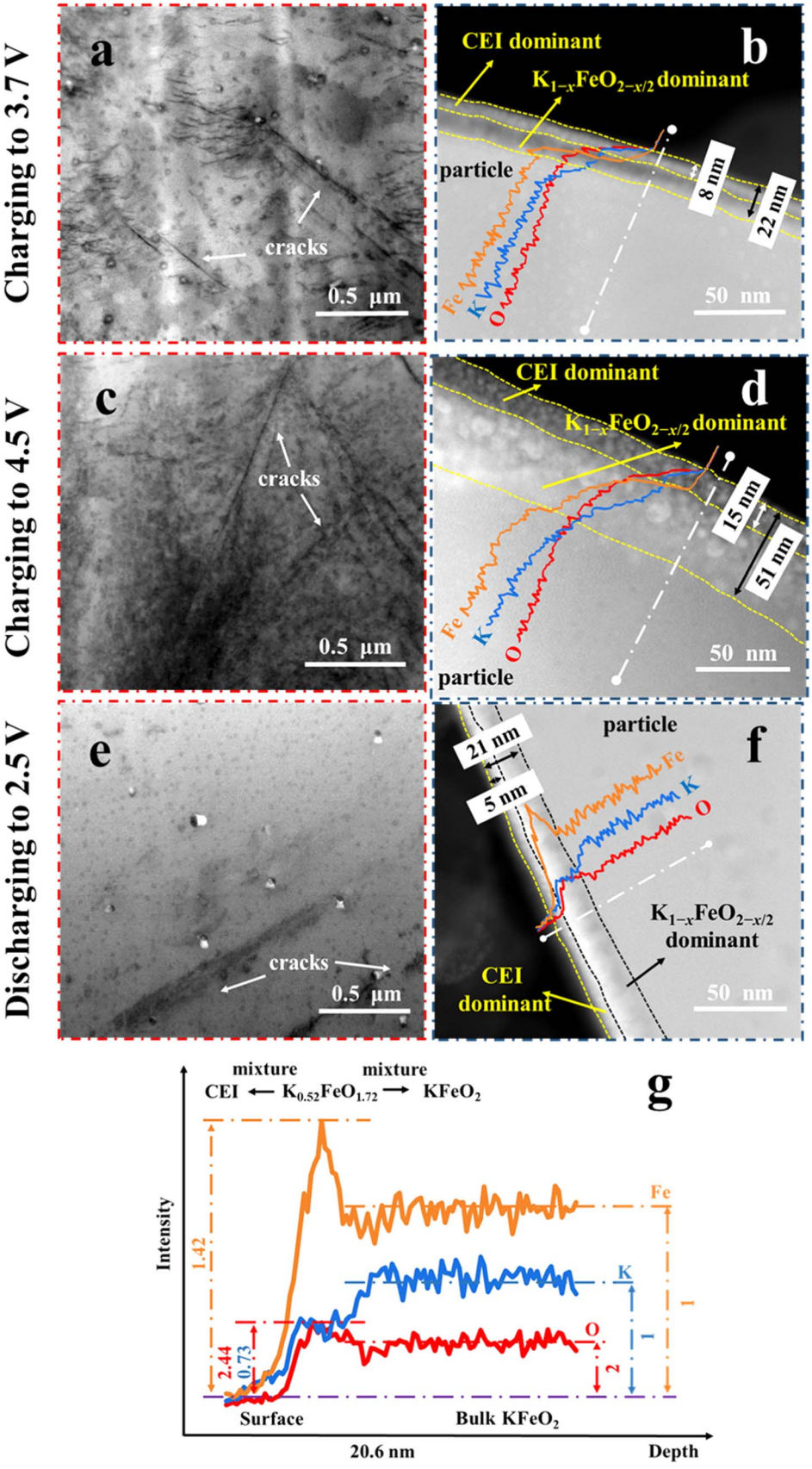

Figure 4. Representative microstructure within a single-particle $KFeO_2$ electrode after charging to 3.7 V, charging to 4.5 V, and discharging to 2.5 V (2.5–3.7 V operation). (a), (c) and (e) TEM images, (b), (d) and (f) EDS images, and (g) elemental composition calculations of $K_{1-x}FeO_{2-x/2}$ based on the composition of bulk $KFeO_2$ (K:Fe:O = 1:1:2) after discharging to 2.5 V.

structural framework identical to $KFeO_2$, indicating the absence of foreign crystal structure evolution. The surface SAED pattern of the sample discharge to 2.5 V indicates polycrystalline nature (Fig. S15), which is assigned to the diffraction index of 102 for $K_2Fe_4O_7$ ($K_{0.5}FeO_{1.75}$)[66] among the various possible iron-based compounds. Although it is difficult to accurately determine the substance of the electrode surface with only one diffraction, the ratio of Fe and O in $K_2Fe_4O_7$ agrees well with the calculated $K_{0.52}FeO_{1.72}$ obtained from

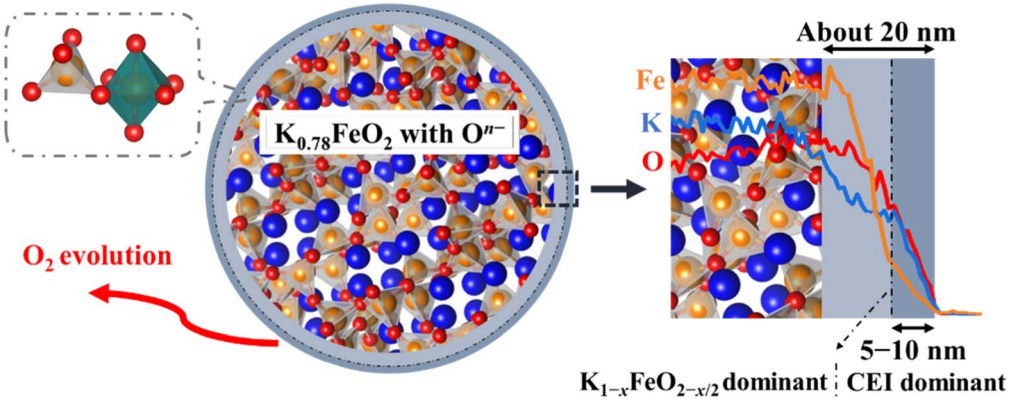

Figure 5. Schematic illustration of the charging mechanism.

EDS analysis. Moreover, the framework of $K_2Fe_4O_7$, which contains both FeO_6 octahedron and FeO_4 tetrahedron,[66] also agrees well with the conclusion made from the soft XAS results, namely the partial transformation from tetrahedral to octahedral.

According to the above analysis results, the reaction of oxygen provides charge compensation during the charge and discharge processes of $KFeO_2$. Furthermore, its electrochemical behavior is affected by a combination of reversible bulk O redox reaction and irreversible surface O oxidation upon K^+ insertion and extraction. Previous research has reported that the Jahn-Teller effect of the formed Fe^{4+} results in the unstable cycling performance of $KFeO_2$.[33] However, our study shows that the irreversible formation of $K_{1-x}FeO_{2-x/2}$ on the surface of the $KFeO_2$ electrode prevents the retransfer of K^+ into the structure with cycling. A schematic illustration of the mechanism of charging to 3.7 V is proposed (Fig. 5), wherein the reaction at the surface region of the $KFeO_2$ particle is as follows:

$$KFeO_2 \rightarrow K_{1-x}FeO_{2-x/2} + x/4\ O_2 + xK^+ + xe^-$$

Conclusions

$KFeO_2$ was successfully synthesized using the solid-state method. The as-synthesized material delivers an initial capacity of 44.3 mAh g^{-1} and 45% capacity retention after 30 cycles between 2.5–3.7 V at a current density of 10 mA g^{-1}. During the charge and discharge processes, the bulk and surface O contribute to the charge compensation through the insertion and extraction of K^+, respectively. The crystallinity of $KFeO_2$ slightly decreases after cycling, which is possibly attributed to the formation of $K_{1-x}FeO_{2-x/2}$ by the irreversible O oxidation reaction on the particle surface. The surface layer mainly composed of $K_{1-x}FeO_{2-x/2}$ blocks the pathways of K^+ transfer from the electrolyte into the structure, which results in an unstable cycle performance. In view of the abundance of Fe in the Earth's crust, more effort should be made to realize the practical application of eco-friendly positive material $KFeO_2$. Several possible methods are raised as follows. First, more redox active sites to improve capacity. Doping with Mn or Ni maybe benefits to large capacity with supplying more active sites, promoting bulk O reaction and stabilizing crystal structure, as their behavior of positive electrode in LIBs and KIBs. Second, stabilize surface O to improve cyclability. Surface coating or doping with Ti may prevent the directly touching of $KFeO_2$ to electrolyte and further avoid irreversible oxidation of surface O.

Acknowledgments

This study was partly supported by the Iwatani Naoji Foundation and ISHIZUE 2023 of Kyoto University. We thank Nippon Shokubai Co., Ltd. for supplying K[FSA] salt. K. Jiao thanks the scholarship support from the Ministry of Education, Culture, Sports, Science, and Technology of Japan (MEXT).

Supplementary Materials

The Supplementary Information is available on the journal website. ICP-AES, EDS, and Rietveld refinement results for pristine $KFeO_2$ powder; photographs of $KFeO_2$ powder before and after exposing in air; XRD patterns of $KFeO_2$ powder synthesized with different excess amount of K_2CO_3; charge–discharge tests with different cut-off voltages; CV, GITT, EIS, XRD, XPS, and TEM results of $KFeO_2$ electrodes at different charge–discharge states (PDF).

ORCID

Takayuki Yamamoto https://orcid.org/0000-0003-3553-3272
Toshiyuki Nohira https://orcid.org/0000-0002-4053-554X

References

1. B. Dunn, H. Kamath, and J. M. Tarascon, *Science*, **334**, 928 (2011).
2. C. Wang, C. Yang, and Z. Zheng, *Adv. Sci.*, **9**, 2105213 (2022).
3. F. Yuan, Z. Li, D. Zhang, Q. Wang, H. Wang, H. Sun, Q. Yu, W. Wang, and B. Wang, *Adv. Sci.*, **9**, 2200683 (2022).
4. S. G. Bratsch, *J. Phys. Chem. Ref. Data*, **18**, 1 (1989).
5. Y. Marcus, *Pure & Appl. Chem.*, **57**, 1129 (1985).
6. J. C. Pramudita, D. Sehrawat, D. Goonetilleke, and N. Sharma, *Adv. Energy Mater.*, **7**, 1602911 (2017).
7. J. Feng, S. Luo, L. Qian, S. Yan, Q. Wang, X. Ji, Y. Zhang, X. Liu, P. Hou, and F. Teng, *Small*, **19**, 2208005 (2023).
8. J. Cong, S. Luo, P. Li, K. Li, P. Li, S. Yan, L. Qian, and X. Liu, *ACS Sustainable Chem. Eng.*, **11**, 16341 (2023).
9. Y. Park, D. Seo, H. Kwon, B. Kim, J. Kim, H. Kim, I. Kim, H. Yoo, and K. Kang, *J. Am. Chem. Soc.*, **135**, 13870 (2013).
10. J. W. Somerville et al., *Energy Environ. Sci.*, **12**, 2223 (2019).
11. W. Luo et al., *Nano Lett.*, **15**, 7671 (2015).
12. Z. Jian, W. Luo, and X. Ji, *J. Am. Chem. Soc.*, **137**, 11566 (2015).
13. Y. Kondo, T. Fukutsuka, K. Miyazaki, Y. Miyahara, and T. Abe, *J. Electrochem. Soc.*, **166**, A5323 (2019).
14. Q. Wang, L. Jiang, Y. Yu, and J. Sun, *Nano Energy*, **55**, 93 (2019).
15. M. Watanabe, M. L. Thomas, S. Zhang, K. Ueno, T. Yasuda, and K. Dokko, *Chem. Rev.*, **117**, 7190 (2017).
16. T. Yamamoto and T. Nohira, *Chem. Rec.*, **23**, e202300169 (2023).
17. T. Yamamoto, R. Matsubara, and T. Nohira, *J. Chem. Eng. Data*, **66**, 1081 (2021).
18. K. Yoshii, T. Masese, M. Kato, K. Kubota, H. Senoh, and M. Shikano, *ChemElectroChem*, **6**, 3901 (2019).
19. T. Yamamoto and T. Nohira, *Chem. Commun.*, **56**, 2538 (2020).
20. H. Onuma et al., *ACS Energy Lett.*, **5**, 2849 (2020).
21. A. Yadav, H. Kobayashi, T. Nikaido, T. Yamamoto, and T. Nohira, *J. Power Sources*, **585**, 233628 (2023).
22. T. Yamamoto, K. Matsumoto, R. Hagiwara, and T. Nohira, *J. Phys. Chem. C*, **121**, 18450 (2017).
23. Y. Domi, H. Usui, E. Nakabayashi, T. Yamamoto, T. Nohira, and H. Sakaguchi, *Electrochemistry*, **87**, 333 (2019).
24. T. Yamamoto, A. Yadav, and T. Nohira, *J. Electrochem. Soc.*, **169**, 050507 (2022).
25. R. D. Shannon, *Acta Crystallogr., Sect. A*, **32**, 751 (1976).
26. T. Hosaka, K. Kubota, A. S. Hameed, and S. Komaba, *Chem. Rev.*, **120**, 6358 (2020).

27. C. Vaalma, G. A. Giffin, D. Buchholz, and S. Passerini, *J. Electrochem. Soc.*, **163**, A1295 (2016).
28. H. Kim, D. Seo, J. C. Kim, S. H. Bo, L. Liu, T. Shi, and G. Ceder, *Adv. Mater.*, **29**, 1702480 (2017).
29. B. Peng, Y. Li, J. Gao, F. Zhang, J. Li, and G. Zhang, *J. Power Sources*, **437**, 226913 (2019).
30. Y. Hironaka, K. Kubota, and S. Komaba, *Chem. Commun.*, **53**, 3693 (2017).
31. H. Kim, J. C. Kim, S.-H. Bo, T. Shi, D.-H. Kwon, and G. Ceder, *Adv. Energy Mater.*, **7**, 1700098 (2017).
32. J.-Y. Hwang, J. Kim, T.-Y. Yu, S.-T. Myung, and Y.-K. Sun, *Energy Environ. Sci.*, **11**, 2821 (2018).
33. S. C. Han, W. B. Park, K. Sohn, and M. Pyo, *J. Solid State Electrochem.*, **23**, 3135 (2019).
34. S. Zhang, J. Sun, J. Gao, W. Jiang, L. Cheng, H. Wang, J. Lin, C. Peng, and J. Wang, *Phys. Chem. Chem. Phys.*, **24**, 4620 (2022).
35. B. Kang and G. Ceder, *Nature*, **458**, 190 (2009).
36. K. Kang, Y. S. Meng, J. Breger, C. P. Grey, and G. Ceder, *Science*, **311**, 977 (2006).
37. W. S. Yoon, K. Y. Chung, X. Yang, J. McBreen, M. Balasubramanian, C. P. Grey, and D. A. Fischer, *J. Am. Chem. Soc.*, **127**, 17479 (2005).
38. G. Ceder, Y. M. Chiang, D. R. Sadoway, M. K. Aydinol, Y. I. Jang, and B. Huang, *Nature*, **392**, 694 (1998).
39. D. H. Seo, J. Lee, A. Urban, R. Malik, S. Y. Kang, and G. Ceder, *Nat. Chem.*, **8**, 692 (2016).
40. A. Grimaud, W. T. Hong, Y. Shao-Horn, and J.-M. Tarascon, *Nat. Mater.*, **15**, 121 (2016).
41. G. Assat and J. M. Tarascon, *Nat. Energy*, **3**, 373 (2018).
42. A. R. Armstrong, M. Holzapfel, P. Novak, C. S. Johnson, S. H. Kang, M. M. Thackeray, and P. G. Bruce, *J. Am. Chem. Soc.*, **128**, 8694 (2006).
43. N. Yabuuchi, K. Yoshii, S. T. Myung, I. Nakai, and S. Komaba, *J. Am. Chem. Soc.*, **133**, 4404 (2011).
44. J. Wu et al., *Sci. Adv.*, **6**, 3871 (2020).
45. D. Susanto, M. K. Cho, G. Ali, J. Kim, H. J. Chang, H. Kim, K. Nam, and K. Y. Chung, *Chem. Mater.*, **31**, 3644 (2019).
46. T. Masese et al., *Energy Technol.*, **8**, 2000039 (2020).
47. F. Izumi and K. Momma, *Solid State Phenom.*, **130**, 15 (2007).
48. K. Momma and F. Izumi, *J. Appl. Crystallogr.*, **44**, 1272 (2011).
49. M. Klinger, *J. Appl. Cryst.*, **50**, 1226 (2017).
50. W. Weppner and R. A. Huggins, *J. Electrochem. Soc.*, **124**, 1569 (1977).
51. C. Delacourt, M. Ati, and J. M. Tarascon, *J. Electrochem. Soc.*, **158**, A741 (2011).
52. L. Liu et al., *ACS Appl. Mater. Interfaces*, **13**, 28369 (2021).
53. X. Zhang, Y. Yang, X. Qu, Z. Wei, G. Sun, K. Zheng, H. Yu, and F. Du, *Adv. Funct. Mater.*, **29**, 1905679 (2019).
54. R. Qiao and W. Yang, *J. Electron. Spectrosc. Relat. Phenom.*, **221**, 58 (2017).
55. Q. Shen, Y. Liu, L. Jiao, X. Qu, and J. Chen, *Energy Storage Mater.*, **35**, 400 (2021).
56. P. S. Miedema and F. M. F. de Groot, *J. Electron. Spectrosc. Relat. Phenom.*, **187**, 32 (2013).
57. N. Yabuuchi et al., *Nat. Commun.*, **7**, 13814 (2016).
58. M. Abbate et al., *Phys. Rev. B*, **46**, 4511 (1992).
59. J. Kim, T. Y. Koo, and J. Park, *Phys. Rev. Lett.*, **96**, 047205 (2006).
60. T. J. Regan, H. Ohldag, C. Stamm, F. Nolting, J. Lüning, J. Stöhr, and R. L. White, *Phys. Rev. B*, **64**, 214422 (2001).
61. K. Kuepper, I. Balasz, H. Hesse, A. Winiarski, K. C. Prince, M. Matteucci, D. Wett, R. Szargan, E. Burzo, and M. Neumann, *Phys. Status Solidi A*, **201**, 3252 (2004).
62. F. M. F. Groot, P. Glatzel, U. Bergmann, P. A. Aken, R. A. Barrea, S. Klemme, M. Halvecker, A. Knop-Gericke, W. M. Heijboer, and B. M. Weckhuysen, *J. Phys. Chem. B*, **109**, 20751 (2005).
63. Y. Chin et al., *Phys. Rev. B*, **99**, 184407 (2019).
64. C. Colliex, T. Manoubi, and C. Ortiz, *Phys. Rev. B*, **44**, 11402 (1991).
65. A. Augustsson, G. V. Zhuang, S. M. Butorin, J. M. Osorio-Guillén, C. L. Dong, R. Ahuja, C. L. Chang, P. N. Ross, J. Nordgren, and J.-H. Guo, *J. Chem. Phys.*, **123**, 184717 (2005).
66. H. Yuan, H. Li, T. Zhang, G. Li, T. He, F. Du, and S. Feng, *J. Mater. Chem. A*, **6**, 8413 (2018).